Accurate Small-Signal Terminal Characteristic Model and SISO Stability Analysis Approach for Parallel Grid-Forming Inverters in Islanded Microgrids

Jiajun Yu, Shike Wang, *Member, IEEE*, Zeng Liu, *Senior Member, IEEE*, Jiarui Li, *Student Member, IEEE*, Jinjun Liu, *Fellow, IEEE*, and Jiayu Shang

***Abstract*—This article derives a small-signal terminal characteristic model for the grid-forming inverter with droop-control in the synchronous reference (*dq*-) frame, accurately covering the dynamics of the power controller, the voltage and current control loops, and all circuit components, where a new set of terminal characteristics is proposed to characterize the small-signal dynamics of fundamental frequency introduced by the fundamental frequency-active power droop scheme. Based on the terminal characteristics of individual inverters, the stability of parallel grid-forming inverters can be predicted by the generalized Nyquist criterion. Furthermore, to simplify the stability analysis process and reduce calculation complexity, a single-input single-output (SISO) stability analysis approach is proposed by exploring the interaction among the droop-control of parallel inverters through analyzing mathematical feature of the proposed terminal characteristic model of individual inverters as well as the return ratio of the parallel inverters, which uses *d-d* channel element of system return ratio matrix and Nyquist criterion to predict the stability. Finally, simulation and experimental results validate the effectiveness of the proposed small-signal model and SISO stability analysis approach.**

***Index Terms*—Fundamental frequency dynamics, grid-forming inverters, impedances, microgrids, small-signal stability.**

I. Introduction

In RECENT years, global warming has become a serious topic attracting close attention worldwide. As an effective solution of mitigating greenhouse gas emissions, renewable energy generation has gained rapid development. Generally, renewable energy sources need power electronic converters as interfaces to connect to the utility grid [1], [2]. For the advantages like high reliability, communication-independent control scheme, plug and play, grid-forming inverters are widely employed as power interfaces in islanded ac microgrids [3], [4], [5].

In order to study the small-signal stability of parallel grid-forming inverters system, the state-space-based approaches are well established in the works of literature [6], [7], [8]. By including the state variables from each individual inverter, the state matrix of overall parallel system is formed, whose eigenvalues reveal the damping of different frequency modes and the system stability. However, the state-space-based approaches are neither computationally efficient nor modular modeling, which is unsuitable for analyzing large networks. Therefore, the impedance-based approach has become the preferable solution for small-signal modeling and stability analysis of ac power electronic systems [9], [10], [11], [13], [14], [15]. Compared to the high-order state matrix, small-signal impedance and admittance are applied to represent the terminal dynamics of power converters, reducing the modeling complexity. Since the impedance model is modularized, it is convenient to rebuild the system model with a change of either the paralleled modules or the network condition. After partitioning the overall system into a source subsystem and a load subsystem, the return-ratio matrix defined by the product of their terminal impedance and admittance can apply the generalized Nyquist stability criterion (GNC) [12], [13] to predict system stability. If each subsystem is stable and with no right-half-plane (RHP) pole in their terminal impedance and admittance, the sufficient and necessary condition for a stable overall system is that the characteristic loci of the return ratio matrix do not encircle the critical point $(-1+j0)$ in the complex plane.

Despite absolute accuracy and no conservatism, the limitations of GNC-based stability analysis are the complex physical interpretation of return ratio matrix and high intricateness of calculating characteristic loci. To overcome the shortage of the GNC in stability analysis, many research works have been done to simplify the multi-input multi-output (MIMO) system and come up with single-input single-output (SISO) stability analysis approaches. In [16] and [17], the stability of three-phase interface under unit power factor (PF) condition can be judged by the Nyquist criterion applying to SISO *d-d* return ratio of

Manuscript received 4 October 2022; revised 1 December 2022; accepted 6 January 2023. Date of publication 17 January 2023; date of current version 10 March 2023. This work was supported by the National Natural Science Foundation of China under Grant 51777160. Recommended for publication by Associate Editor H. H.-C. Iu. *(Corresponding author: Zeng Liu.)*

Jiajun Yu, Zeng Liu, Jiarui Li, Jinjun Liu, and Jiayu Shang are with the State Key Laboratory of Electrical Insulation and Power Equipment, School of Electrical Engineering, Xi'an Jiaotong University, Xi'an 710049, China (e-mail: y1055130561@stu.xjtu.edu.cn; zengliu@mail.xjtu.edu.cn; ljr19990825@stu.xjtu.edu.cn; jjliu@mail.xjtu.edu.cn; shangjy@stu.xjtu.edu.cn).

Shike Wang was with the State Key Laboratory of Electrical Insulation and Power Equipment, School of Electrical Engineering, Xi'an Jiaotong University, Xi'an 710049, China. She is now with the China Resources Power Technology Research Institute Co., Ltd., Shenzhen 518001, China (e-mail: wangshike@crpower.com.cn).

Color versions of one or more figures in this article are available at https://doi.org/10.1109/TPEL.2023.3237599.

Digital Object Identifier 10.1109/TPEL.2023.3237599

impedance and admittance. In [18], the initial MIMO small-signal model of grid-connected inverter is resolved in three SISO systems, which represents the dynamics of ac-bus-voltage control, current control and dc-bus-voltage control, and the overall system stability is assessed by applying Nyquist criterion to each SISO subsystems, respectively. In [19], a three-phase ac system, where tightly regulated power converters are equipped with decoupled *dq*-domain controllers, can then be treated as two decoupled dc systems in *d*-*d* and *q*-*q* channel. In [20], the unified impedance network model of power converters, turbo generators, and line commutated converters in high-voltage direct current system are built successively, and then aggregated into a lumped impedance matrix. The system stability is evaluated by observing the impedance-frequency curves of the determinant of the lump matrix, which is applicable for very large scale power systems. In [21], the possible location of characteristic loci is found to lie in two band areas according to the Gershgorin theorem, and the system can be stable by ensuring that the two band areas do not encircle or cover the critical point (–1+j0). The simplified criterion proposed in [21] uses the diagonal and off-diagonal elements of the return ratio matrix directly and can avoid the computation of characteristic loci. Although these SISO approaches are strictly sufficient in certain conditions, for example, in condition of grid-connected inverters operating at high PF, they may lose the accuracy and applicability when applied to parallel inverter system in stand-alone operation, since the characteristics of stand-alone parallel system have not been fully discussed.

As for the parallel grid-forming inverters, relevant works on small-signal impedance modeling and stability analysis have been presented [22], [23], [24], [25], [26], [27], [28], [29]. A typical grid-forming control scheme consists of the outer power controller implemented by the droop-control or the virtual synchronous generator control, inner capacitor voltage, and inductor current dual loops. Moreover, if the *LC* filter and distribution cable are considered, the impedance model of the grid-forming inverter will be very complicated, covering the dynamics of three control loops and passive components. In the reduced-order small-signal impedance models presented in [22] and [23], the inner capacitor voltage and inductor current control loops of the grid-forming inverter are neglected and regarded as a unit gain block in the modeling process. However, these impedance models are simplified and inevitably neglect some critical dynamics introduced by the inner voltage controller [8], [27]. Therefore, even in static load conditions, the impedance models neglecting inner control loops in [22] and [23] are not able to accurately characterize the comprehensive terminal dynamics of grid-forming inverters. When supplying motor loads or nonlinear loads, the system stability is influenced by the interactions between loads and the inverter within medium- or harmonic-frequency range. Considering the bandwidth separation between relatively slow power droop-control and inner dual-loop control, the effect of the outer power controller is ignored by setting droop slopes m_p, n_q to zero [24], [25], [26]. In this kind of small-signal impedance model, the coupling effects of active and reactive power cannot be reflected. Moreover, the small-signal dynamic of the fundamental frequency is neglected. For parallel grid-forming inverters, the dynamics of power sharing and fundamental frequency synchronizations between multiple inverters cannot be described without considering the outer power controller.

In order to compensate the limitations of impedance models in [22], [23], [24], [25], and [26] and characterize the comprehensive dynamics of grid-forming inverters, a comprehensive definition of small-signal terminal characteristics is proposed in [28]. Besides conventional impedance and admittance, a new set of terminal characteristics is proposed to represent the fundamental frequency dynamics considering the fundamental frequency-active power droop scheme. Based on the terminal characteristics of individual inverters, the small-signal model of parallel grid-forming inverters with a single ac bus is constructed. Then, a GNC-based stability criterion is proposed to predict the stability of the parallel system. After introducing the terminal characteristics of the grid-forming inverter proposed in [28] into the modeling of a multiple-bus ac microgrid, a stability analysis based on the component connection method is presented in [29].

In [28], the overall definition of small-signal terminal characteristics of grid-forming inverter is just proposed. Neither analytical model nor specific transfer functions are provided. Thus, the stability analyses in [28] and [29] rely on the frequency-sweep measurement results, where additional perturbation injection and signal processing procedures are required. Meanwhile, the GNC-based stability criterion in [28] is of poor practicability due to its MIMO nature. The intricateness of calculating characteristic loci makes it highly impracticable to establish a clear link between parameter changes and system stability.

As a continuation of [28], this article fills the gap of building a full analytical small-signal model with the proposed new characteristics and provides a SISO stability analysis approach for parallel grid-forming inverters. First, an accurate analytical model of small-signal terminal characteristics is derived in *dq*-frame by including the dynamics of outer power controller and inner capacitor voltage and inductor current controllers, as well as the *LC* filter and other circuit components. Second, the interaction among the droop-control of the grid-forming inverters in parallel is investigated by analyzing the mathematical feature of the analytical terminal characteristics of individual inverters as well as the return ratio of parallel system. Then, it is revealed that the characteristic loci of the parallel grid-forming inverters can further be simplified and a SISO stability analysis approach for the parallel system is proposed based on the Gershgorin theorem. Furthermore, the comparisons between the proposed accurate model and existing simplified small-signal models, presented in [22], [23] and [24], [25], [26], are conducted, and it is found that some critical dynamics cannot be reflected in the simplified models, which leads to incorrect stability predictions. Meanwhile, the comparison between stability predicting results of the proposed SISO stability criterion and the stability criterion presented in [21] is also conducted, and it is noted that the criterion in [21] may fail to offer a correct prediction since the characteristics of the islanded system are different comparing to the grid-connected system.

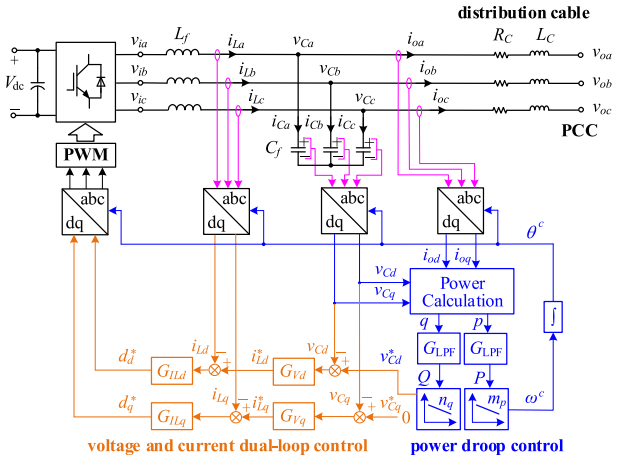

Fig. 1. Block diagram of a typical three-phase grid-forming inverter.

The rest of this article is organized as follows. Section II illustrates the modeling process of small-signal terminal characteristics of a single grid-forming inverter. Section III develops the SISO stability analysis approach for parallel grid-forming inverters. Section IV studies the stability of the parallel system in different cases and compares the proposed accurate model and stability criterion with existing models and simplified criterion. Terminal characteristic measurement and experimental results are presented in Section V to validate the theoretical analysis. Finally, Section VI concludes the article.

II. Accurate Small-Signal Terminal Characteristics Model of Grid-Forming Inverters

In this section, the operation principle of a grid-forming inverter with power stage and three control loops is first introduced in Section II-A. Then, the complete small-signal model considering the dynamic of each part is established in the individual synchronous reference frame (SRF) of each inverter as discussed in Section II-B to Section II-D. Finally, the above model is transformed to a common SRF considering the coupling effect introduced by frame dynamic as shown in Section II-E.

A. Operation Principle of Grid-Forming Inverter

The block diagram of a typical three-phase grid-forming inverter is shown in Fig. 1 [3], [4]. In power stage, the renewable energy sources usually feed in dc side, where extra strategy is applied to maintain a stiff dc voltage. The *LC* filter in ac side is adopted to filter the switching ripples, whose output terminal is tied to the point of common coupling (PCC) through a distribution cable with the resistance R_C and inductance L_C. As Fig. 1 shows, the droop-control scheme is implemented in the outer power controller. In *dq*-frame, the instantaneous output active and reactive powers of the inverter are calculated as follows:

$$p = \frac{3}{2}\left(v_{Cd}i_{od} + v_{Cq}i_{oq}\right), \quad q = \frac{3}{2}\left(-v_{Cd}i_{oq} + v_{Cq}i_{od}\right). \tag{1}$$

To obtain the fundamental components of output power, P and Q, a first-order low-pass filter (LPF) is usually applied

$$P = G_{\mathrm{LPF}}p, \quad Q = G_{\mathrm{LPF}}q$$
$$G_{\mathrm{LPF}} = \frac{\omega_f}{s+\omega_f} \tag{2}$$

where ω_f is the cutoff frequency of the power LPF.

Based on the droop scheme, the references of fundamental frequency and capacitor voltage amplitude are regulated as

$$\omega^c = \omega_0 - m_p(P - P_0), \quad v_{Cd}^* = V_0 - n_q(Q - Q_0) \tag{3}$$

where m_p and n_q are active and reactive power droop slopes, m_p, n_q >0, and P_0 and Q_0 are output power biases at rated fundamental frequency ω_0 and voltage amplitude V_0.

As mentioned before, the accurate terminal characteristic model of a grid-forming inverter covers the dynamics of outer power controller, inner voltage and current dual loops, and passive components including *LC* filter and distribution cable. In the following sections, the small-signal models of three control loops and the power stage are built successively, which are finally combined together to derive the analytical expressions of the overall terminal characteristics.

B. Small-Signal Modeling of Inner Voltage and Current Loops

As Fig. 1 shows, the control schemes are implemented in the SRF whose rotating frequency ω^c is generated in (3). In the modeling process, the small-signal variables under this inverter individual SRF are marked by superscript c, which denotes controller frame.

Based on Fig. 1, the small-signal model of inner capacitor voltage and inductor current dual loops, including the dynamics of pulsewidth modulation (PWM) modulation and *LC* filter, is depicted in Fig. 2. In Fig. 2, the voltage reference $\hat{\mathbf{v}}_{Cdq}^{*c}$ is generated by outer control loop. The capacitor voltage control is achieved with a PI controller, of which the transfer function matrix in *dq*-frame is represented by $\mathbf{G}_V$ in (4). The inductor current controller is not dominant, which is applied to damp the resonance of *LC* filter and improve the dynamic performance. A simple P controller $\mathbf{G}_{IL}$ as shown in (4) is usually adopted. The output of current controller $\hat{\mathbf{d}}_{dq}^{*c}$ is regarded as the reference for PWM modulation. Since this article focuses on the low- and medium-frequency behavior of grid-forming inverter, computational and PWM time delays are ignored in the small-signal modeling process. Meanwhile, the dc voltage V_{dc} is controlled to be unchanged. Thus, the dynamics from dc side is neglected. As shown in (4), a constant matrix $\mathbf{G}_{\mathrm{PWM}}$ is used to represent the PWM modulation effect

$$\mathbf{G}_V = \begin{bmatrix} k_{pv} + k_{iv}/s & 0 \\ 0 & k_{pv} + k_{iv}/s \end{bmatrix}, \quad \mathbf{G}_{IL} = \begin{bmatrix} k_{pc} & 0 \\ 0 & k_{pc} \end{bmatrix}$$
$$\mathbf{G}_{\mathrm{PWM}} = \begin{bmatrix} V_{\mathrm{dc}}/2 & 0 \\ 0 & V_{\mathrm{dc}}/2 \end{bmatrix} \tag{4}$$

where k_{pv} and k_{iv} are the proportional gain and integral gain of voltage controller, and k_{pc} is the proportional gain of current controller.

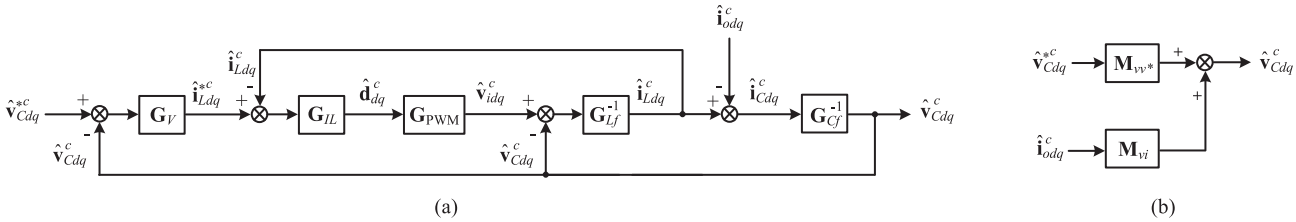

Fig. 2. Small-signal model of inner capacitor voltage and inductor current control loops in inverter individual SRF in forms of (a) complete block diagram and (b) equivalent block diagram.

In Fig. 1, the output voltage of three-phase half-bridge is named as v_{iabc}. Based on Kirchhoff's circuit laws, the equations between v_{iabc}, capacitor voltage v_{Cabc}, inductor current i_{Labc}, capacitor current i_{Cabc}, and output terminal current i_{oabc} can be derived as

$$L_f \frac{\mathrm{d}i_{Labc}}{\mathrm{d}t}\mathrm{d}t + r_{Lf} \cdot i_{Labc} = v_{iabc} - v_{Cabc}$$

$$C_f \frac{\mathrm{d}v_{Cabc}}{\mathrm{d}t} = i_{Cabc} = i_{Labc} - i_{oabc} \tag{5}$$

where r_{Lf} is the equivalent series resistance (ESR) of filter inductor L_f. Since film capacitor is generally used as filter capacitor C_f, ESR at the fundamental frequency is very small and can be neglected.

After converting to *dq*-frame, (5) can be written as

$$\begin{cases} L_f \frac{\mathrm{d}i_{Ld}}{\mathrm{d}t} - \omega^c L_f \cdot i_{Lq} + r_{Lf} \cdot i_{Ld} = v_{id} - v_{Cd} \\ L_f \frac{\mathrm{d}i_{Lq}}{\mathrm{d}t} + \omega^c L_f \cdot i_{Ld} + r_{Lf} \cdot i_{Lq} = v_{iq} - v_{Cq} \end{cases} \tag{6}$$

$$\begin{cases} C_f \frac{\mathrm{d}v_{Cd}}{\mathrm{d}t} - \omega^c C_f \cdot v_{Cq} = i_{Ld} - i_{od} \\ C_f \frac{\mathrm{d}v_{Cq}}{\mathrm{d}t} + \omega^c C_f \cdot v_{Cd} = i_{Lq} - i_{oq}. \end{cases} \tag{7}$$

Conducting the small-signal linearization on (6) to (7), (8) and (9) are obtained as

$$\mathbf{G}_{Lf} \cdot \hat{\mathbf{i}}^c_{Ldq} = \hat{\mathbf{v}}^c_{idq} - \hat{\mathbf{v}}^c_{Cdq}$$

$$\mathbf{G}_{Lf} = \begin{bmatrix} sL_f + r_{Lf} & -\Omega^c L_f \\ \Omega^c L_f & sL_f + r_{Lf} \end{bmatrix} \tag{8}$$

$$\mathbf{G}_{Cf} \cdot \hat{\mathbf{v}}^c_{Cdq} = \hat{\mathbf{i}}^c_{Ldq} - \hat{\mathbf{i}}^c_{odq}$$

$$\mathbf{G}_{Cf} = \begin{bmatrix} sC_f & -\Omega^c C_f \\ \Omega^c C_f & sC_f \end{bmatrix} \tag{9}$$

where Ω^c represents the steady-state value of ω^c at a certain operating point.

Based on Fig. 2, the transfer functions between $\hat{\mathbf{v}}^{*c}_{Cdq}$ and $\hat{\mathbf{i}}^c_{odq}$, $\hat{\mathbf{v}}^c_{Cdq}$ can be derived as (10), where the transfer functions of inner voltage and current dual loops as well as *LC* filter are represented by $\mathbf{M}$

$$\hat{\mathbf{v}}^c_{Cdq} = \mathbf{M}_{vv*} \cdot \hat{\mathbf{v}}^{*c}_{Cdq} + \mathbf{M}_{vi} \cdot \hat{\mathbf{i}}^c_{odq} \tag{10}$$

where

$$\mathbf{T} = \mathbf{G}_{\mathrm{PWM}} \cdot \mathbf{G}_{IL} \cdot (\mathbf{G}_V + \mathbf{G}_{Cf}) + \mathbf{G}_{Lf} \cdot \mathbf{G}_{Cf} + \mathbf{I}$$

$$\mathbf{M}_{vv*} = \mathbf{T}^{-1} \cdot \mathbf{G}_{\mathrm{PWM}} \cdot \mathbf{G}_{IL} \cdot \mathbf{G}_V$$

$$\mathbf{M}_{vi} = -\mathbf{T}^{-1} \cdot (\mathbf{G}_{Lf} + \mathbf{G}_{\mathrm{PWM}} \cdot \mathbf{G}_{IL}).$$

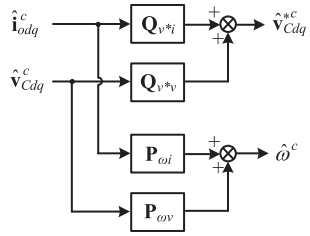

Fig. 3. Small-signal model of the outer power controller in inverter individual SRF.

$\mathbf{M}_{vi}$ is the terminal impedance without considering the dynamics of outer power controller and distribution cable.

C. Small-Signal Modeling of Outer Power Controller

The outer power controller functions the droop-control scheme, achieving power sharing and synchronization between inverters in parallel condition. After applying small-signal linearization to (1)–(3), the small-signal model of the outer power controller can be depicted in Fig. 3. The transfer functions of *P*–ω droop-control and *Q*–*V* droop-control are represented by $\mathbf{P}$ and $\mathbf{Q}$, respectively, as shown in (11) and (12)

$$\mathbf{P}_{\omega i} = \begin{bmatrix} -\frac{3m_p V^c_{Cd} G_{\mathrm{LPF}}}{2} & -\frac{3m_p V^c_{Cq} G_{\mathrm{LPF}}}{2} \end{bmatrix}$$

$$\mathbf{P}_{\omega v} = \begin{bmatrix} -\frac{3m_p I^c_{od} G_{\mathrm{LPF}}}{2} & -\frac{3m_p I^c_{oq} G_{\mathrm{LPF}}}{2} \end{bmatrix} \tag{11}$$

$$\mathbf{Q}_{v*i} = \begin{bmatrix} -\frac{3n_q V^c_{Cq} G_{\mathrm{LPF}}}{2} & \frac{3n_q V^c_{Cd} G_{\mathrm{LPF}}}{2} \\ 0 & 0 \end{bmatrix}$$

$$\mathbf{Q}_{v*v} = \begin{bmatrix} \frac{3n_q I^c_{oq} G_{\mathrm{LPF}}}{2} & -\frac{3n_q I^c_{od} G_{\mathrm{LPF}}}{2} \\ 0 & 0 \end{bmatrix} \tag{12}$$

where V^c_{Cd} and V^c_{Cq} are steady-state capacitor voltages, and I^c_{od} and I^c_{oq} are steady-state output currents. All of these steady-state values are represented in inverter individual SRF. In most cases, the q-axis voltage reference v^{*c}_{Cq} is fixed as 0. Therefore, the elements in the second line of $\mathbf{Q}_{v^*i}$ and $\mathbf{Q}_{v^*v}$ are always equal to 0.

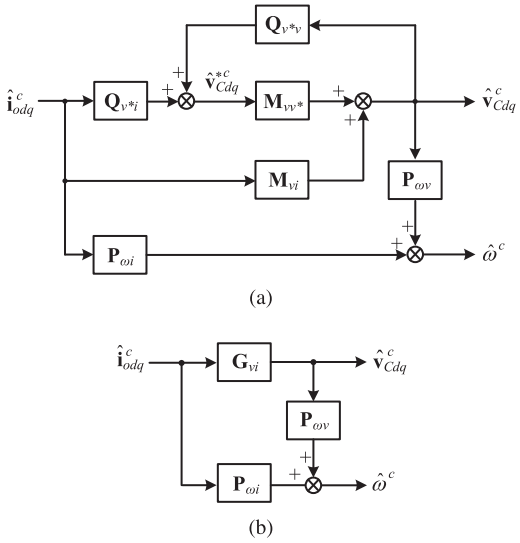

Fig. 4. Terminal characteristics without distribution cable in inverter individual SRF in forms of (a) complete block diagram and (b) equivalent block diagram.

D. Complete Terminal Characteristics Represented in Inverter Individual SRF

By combining the small-signal model of inner dual loops and the outer power controller, the small-signal terminal characteristics of a single grid-forming inverter without considering the distribution cable can be depicted as Fig. 4. In Fig. 4, $\mathbf{G}_{vi}$ can be regarded as the terminal impedance of the single grid-forming inverter without cable, characterizing the dynamic interaction from the excitation of output current to its response of inverter output voltage on filter capacitor. The transfer function is derived in the following equation:

$$\mathbf{G}_{vi} = (\mathbf{I} - \mathbf{M}_{vv*} \cdot \mathbf{Q}_{v*v})^{-1} \cdot (\mathbf{M}_{vv*} \cdot \mathbf{Q}_{v*i} + \mathbf{M}_{vi}). \quad (13)$$

As mentioned before, the overall small-signal terminal characteristic model includes the dynamics of the distribution cable. According to Fig. 1, based on Kirchhoff's circuit laws, the equation between capacitor voltage v_{Cabc}, PCC voltage v_{oabc}, and output current i_{oabc} is derived as

$$L_C \frac{\mathrm{d}i_{oabc}}{\mathrm{d}t} + R_C \cdot i_{oabc} = v_{Cabc} - v_{oabc}. \quad (14)$$

After converting to *dq*-frame and the small-signal linearization, (14) can be expressed as follows:

$$\mathbf{G}_{ZC} \cdot \hat{\mathbf{i}}^c_{odq} = \hat{\mathbf{v}}^c_{Cdq} - \hat{\mathbf{v}}^c_{odq}$$
$$\mathbf{G}_{ZC} = \begin{bmatrix} sL_C + R_C & -\Omega^c L_C \\ \Omega^c L_C & sL_C + R_C \end{bmatrix}. \quad (15)$$

Fig. 5 shows an *N* parallel grid-forming inverter system. As discussed in [28], the parallel inverters are divided into two groups: Inv #1 functions as a voltage source and is described with the small-signal terminal characteristics of voltage representation, whereas Invs #2 to #*N* function as current sources and are described with the small-signal terminal characteristics of current representation.

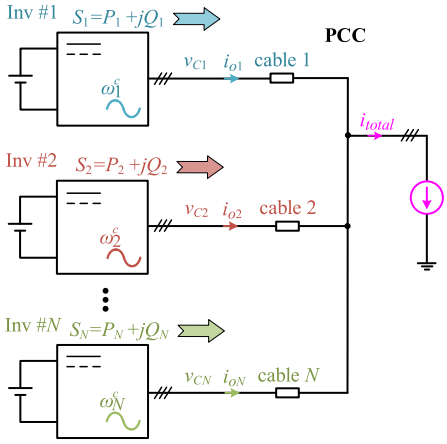

Fig. 5. Configuration of *N* parallel grid-forming inverters.

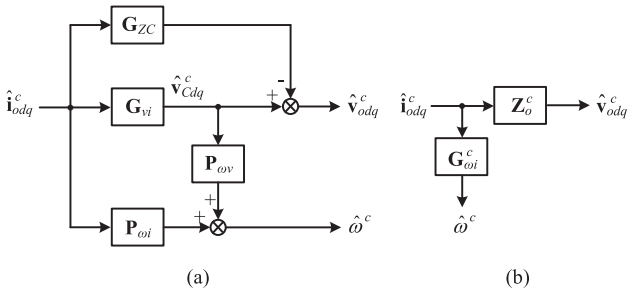

Fig. 6. Terminal characteristics of Inv #1 in inverter individual SRF in forms of (a) complete block diagram and (b) equivalent block diagram.

For Inv #1, the output voltage at PCC $\hat{\mathbf{v}}^c_{odq}$ is regarded as output response. The complete terminal characteristics considering the dynamic of distribution cable are depicted in Fig. 6. In Fig. 6(b), $\mathbf{Z}^c_o$ is the terminal impedance of the grid-forming inverter in voltage representation. $\mathbf{G}^c_{\omega i}$ characterizes the dynamic interaction from the excitation of output current to its response of fundamental frequency. Both two transfer functions are represented in inverter individual SRF with the superscript *c*. The expressions of two transfer functions are shown in (16) and (17)

$$\mathbf{Z}^c_o = \mathbf{G}_{vi} - \mathbf{G}_{ZC} \quad (16)$$
$$\mathbf{G}^c_{\omega i} = \mathbf{P}_{\omega i} + \mathbf{P}_{\omega v} \cdot \mathbf{G}_{vi}. \quad (17)$$

For Invs #2 to #*N*, $\hat{\mathbf{v}}^c_{odq}$ is regarded as an external excitation. The complete terminal characteristics are depicted in Fig. 7. $\mathbf{Y}^c_o$ is the terminal admittance of the grid-forming inverter in current representation.

In inverter individual SRF, the block diagram in Fig. 7(b) is an equivalent form of that in Fig. 6(b) and $\mathbf{Y}^c_o$ should be the inverse of $\mathbf{Z}^c_o$as shown in the following equation:

$$\mathbf{Y}^c_o = (\mathbf{Z}^c_o)^{-1}. \quad (18)$$

It is noted that only the dynamic of *Q*–*V* droop-control is embedded into the terminal impedance and admittance $\mathbf{Z}^c_o$ and

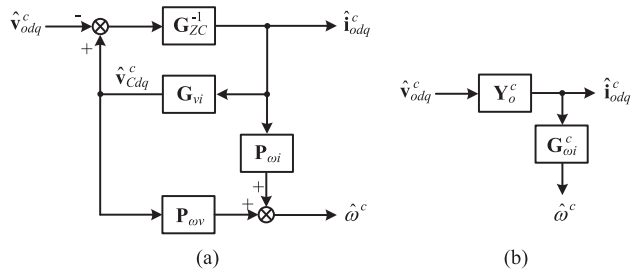

Fig. 7. Terminal characteristics of Inv #2 to #*N* in inverter individual SRF in forms of (a) complete block diagram and (b) equivalent block diagram.

$\mathbf{Y}_o^c$, whereas the dynamic of *P*–ω droop-control is described by the new defined terminal characteristic $\mathbf{G}_{\omega i}^c$.

E. Complete Terminal Characteristics Represented in System SRF

Above small-signal models and expressions are derived in inverter individual SRF whose rotating frequency ω^c is generated by the droop scheme in (3). In an *N* parallel grid-forming inverter system, each inverter generates its own $\omega_1^c,\ \ldots, \omega_N^c$. In order to construct the overall small-signal model of parallel system and analyze the stability, all circuit variables must be transformed to one common SRF. The SRF aligned to PCC voltage is taken as the common SRF in this article. Assuming the rotating frequency of this common SRF is ω^s. The variables under the common SRF are marked by superscript *s*, which denotes the system frame. The angle difference between inverter individual SRF and system SRF can be defined as

$$\delta = \delta_0 + \int (\omega^c - \omega^s)\mathrm{d}t, \qquad \widehat{\delta} = \frac{(\hat{\omega}^c - \hat{\omega}^s)}{s} \tag{19}$$

where δ_0 represents the steady-state leading angle of inverter individual SRF comparing to the system SRF.

Since the transformation calculation of *dq*-circuit variables in different SRFs has already been elaborated in [7] and [8], the small-signal transfer functions of *dq*-capacitor voltage and output current in inverter individual SRF and system SRF are directly presented as

$$\begin{aligned} \hat{\mathbf{v}}_{odq}^c &= \mathbf{T}_s^{-1}(\delta_0)\hat{\mathbf{v}}_{odq}^s + \mathbf{T}_v\widehat{\delta} \\ \hat{\mathbf{i}}_{odq}^s &= \mathbf{T}_s(\delta_0)\hat{\mathbf{i}}_{odq}^c + \mathbf{T}_c\widehat{\delta} \end{aligned} \tag{20}$$

where

$$\mathbf{T}_s(\delta_0) = \begin{bmatrix} \cos(\delta_0) & -\sin(\delta_0) \\ \sin(\delta_0) & \cos(\delta_0) \end{bmatrix}$$

$$\mathbf{T}_v = \begin{bmatrix} -V_{od}^s\sin(\delta_0) + V_{oq}^s\cos(\delta_0) \\ -V_{od}^s\cos(\delta_0) - V_{oq}^s\sin(\delta_0) \end{bmatrix}$$

$$\mathbf{T}_c = \begin{bmatrix} -I_{od}^c\sin(\delta_0) - I_{oq}^c\cos(\delta_0) \\ I_{od}^c\cos(\delta_0) - I_{oq}^c\sin(\delta_0) \end{bmatrix}.$$

V_{od}^s and V_{oq}^s are steady-state output voltages in system SRF.

For Inv #1, the reference fundamental frequency equals to its individual frequency,$\omega^s = \omega_1^c$. The small-signal terminal characteristics in Fig. 6(b) can be transformed to system SRF by (19) and (20) as shown in Fig. 8, noticing that $\hat{\delta} = 0$. The superscript *s* of the transfer functions in system SRF is omitted.

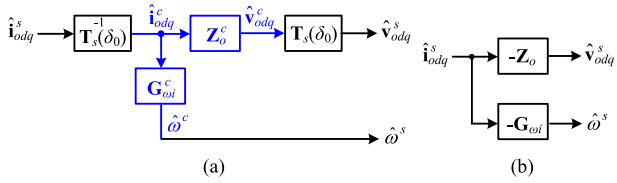

Fig. 8. Terminal characteristics of Inv #1 in system SRF in forms of (a) complete block diagram and (b) equivalent block diagram.

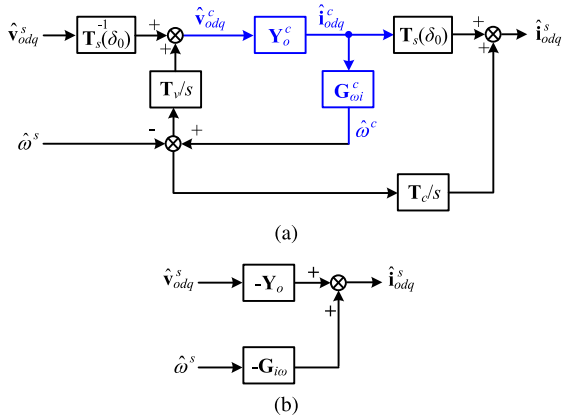

Fig. 9. Terminal characteristics of Inv #2 to #*N* in system SRF in forms of (a) complete block diagram and (b) equivalent block diagram.

As shown in Fig. 8, the inverter output current $\hat{\mathbf{i}}_{odq}^s$ is regarded as an external excitation for Inv #1. The reference fundamental frequency $\hat{\omega}^s$ and output voltage at PCC $\hat{\mathbf{v}}_{odq}^s$ are regarded as output responses. Besides traditional output impedance $\mathbf{Z}_o$, a novel terminal characteristic $\mathbf{G}_{\omega i}$ is proposed to characterize the dynamic interaction from the excitation of current to its response of fundamental frequency [28]. Since the conventional definition of small-signal terminal characteristics requires the direction of current to be input [13], [14], [15], there exists a minus before $\mathbf{Z}_o$ and $\mathbf{G}_{\omega i}$ in Fig. 8. The expressions of the transfer functions are shown in (21) and (22)

$$\mathbf{Z}_o = -\mathbf{T}_s(\delta_0)\cdot\mathbf{Z}_o^c\cdot\mathbf{T}_s^{-1}(\delta_0) \tag{21}$$

$$\mathbf{G}_{\omega i} = -\mathbf{G}_{\omega i}^c\cdot\mathbf{T}_s^{-1}(\delta_0). \tag{22}$$

For Invs #2 to #*N*, the reference fundamental frequency ω^s is irrelevant to the individual frequency ω_k^c, $\hat{\delta}_k \neq 0$, $k = 2, 3, \ldots, N$. The small-signal terminal characteristics in Fig. 7(b) can therefore be transformed to system SRF by (19) and (20), as shown in Fig. 9.

In Fig. 9, the reference fundamental frequency $\hat{\omega}^s$ and PCC voltage $\hat{\mathbf{v}}_{odq}^s$ are regarded as external excitations, whereas the inverter output current $\hat{\mathbf{i}}_{odq}^s$ is output response. Besides traditional input admittance $\mathbf{Y}_o$, a new terminal characteristic $\mathbf{G}_{i\omega}$ describes the small-signal dynamic interaction between the fundamental frequency perturbation and the current response [28]. Due to the direction of current being output in Fig. 9, similar to $\mathbf{Z}_o$ and $\mathbf{G}_{\omega i}$,

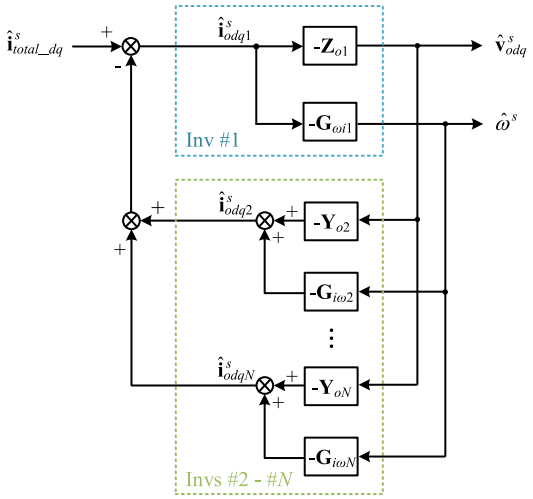

Fig. 10. Small-signal model of *N* parallel grid-forming inverters.

there also exists a minus before $\mathbf{Y}_o$ and $\mathbf{G}_{i\omega}$. The expressions of the transfer functions are shown in (23) and (24)

$$\mathbf{Y}_o = -(\mathbf{T}_s(\delta_0)\cdot\mathbf{Y}_o^c\cdot\mathbf{T}_s^{-1}(\delta_0) + \frac{(\mathbf{T}_s(\delta_0)\cdot\mathbf{Y}_o^c\cdot\mathbf{T}_v+\mathbf{T}_c)\cdot\mathbf{G}_{\omega i}^c\cdot\mathbf{Y}_o^c\cdot\mathbf{T}_s^{-1}(\delta_0)}{s-\mathbf{G}_{\omega i}^c\cdot\mathbf{Y}_o^c\cdot\mathbf{T}_v}) \tag{23}$$

$$\mathbf{G}_{i\omega} = \frac{\mathbf{T}_s(\delta_0)\cdot\mathbf{Y}_o^c\cdot\mathbf{T}_v+\mathbf{T}_c}{s-\mathbf{G}_{\omega i}^c\cdot\mathbf{Y}_o^c\cdot\mathbf{T}_v}. \tag{24}$$

III. SISO Stability Analysis Approach for Parallel Grid-Forming Inverters

A. System Studied and GNC-Based Criterion

For *N* parallel grid-forming inverters depicted in Fig. 5, the small-signal model of the overall system and a stability prediction criterion have been proposed in [28] based on the terminal characteristics of individual inverters.

As shown in Fig. 10, the output current of Inv #1 $\hat{\mathbf{i}}_{odq1}^s$ is decided by the output currents of Invs #2 to #*N* $\hat{\mathbf{i}}_{odq2}^s$, …, $\hat{\mathbf{i}}_{odqN}^s$, and further perturbs the amplitude and frequency of PCC voltage $\hat{\mathbf{v}}_{odq}^s$ and $\hat{\omega}^s$. For Invs #2 to #*N*, $\hat{\mathbf{v}}_{odq}^s$ and $\hat{\omega}^s$ also perturb the output currents $\hat{\mathbf{i}}_{odq2}^s$, …, $\hat{\mathbf{i}}_{odqN}^s$. In this way, the interaction loops of voltage and current as well as frequency and current are formed.

Using GNC [12], [13], the system return ratio matrix $\mathbf{L}$ is defined as (25) based on Fig. 10

$$\mathbf{L} = \sum_{k=2}^{N}(\mathbf{Y}_{ok}\cdot\mathbf{Z}_{o1}+\mathbf{G}_{i\omega k}\cdot\mathbf{G}_{\omega i1}) = \begin{bmatrix} L_{dd} & L_{dq} \\ L_{qd} & L_{qq}\end{bmatrix}. \tag{25}$$

Since this article focuses on the small-signal stability issues related to dynamic interactions between parallel grid-forming inverters, two statements must be emphasized here. First, RHP pole should not exist in the transfer functions of $\mathbf{Z}_{o1}$, $\mathbf{G}_{\omega i1}$ and $\mathbf{Y}_{ok}$, $\mathbf{G}_{i\omega k}$, $k = 2, \ldots, N$, which is a prerequisite for parameter design of individual inverters. It would be meaningless to study the stability of parallel system if there already existed unstable single module. Second, since only the dynamics of grid-forming inverters are concerned, the dynamics of loads are excluded. As Fig. 5 shows, the external load connected to PCC is regarded as an ideal current sink that does not affect system stability. Consequently, according to GNC, the sufficient and necessary condition for a stable parallel system is that the characteristic loci of the return ratio matrix $\mathbf{L}$ do not encircle the critical point $(-1+\mathrm{j}0)$ in the complex plane.

However, despite the absolute accuracy of stability prediction, this GNC-based stability criterion is very complex and cannot provide clear insight into the system stability analysis. Addressing the need for a more practical stability analysis approach, the GNC-based criterion will be simplified based on theoretical analysis to the characteristics of the return ratio matrix in this section.

B. Influence of Droop-Control on System Return Ratio

1) Simplification of Terminal Characteristic Model of Individual Inverter: For the convenience of the following explanation, two major simplifications to the terminal characteristic model established in Section II will be adopted.

First, as mentioned before, the dynamic of *P*–ω droop-control can be studied by the terminal characteristic $\mathbf{G}_{\omega i}^c$, whereas the dynamic of *Q*–*V* droop-control is embedded in the terminal impedance $\mathbf{G}_{vi}$. To gain a better insight into the effect of the *Q*–*V* droop-control on the terminal characteristics, $\mathbf{G}_{vi}$ can be further simplified by two steps from (13) to (26) as follows:

$$\begin{aligned}\mathbf{G}_{vi} &\approx (\mathbf{I}+\mathbf{M}_{vv*}\cdot\mathbf{Q}_{v*v})\cdot(\mathbf{M}_{vv*}\cdot\mathbf{Q}_{v*i}+\mathbf{M}_{vi}) \\ &\approx \mathbf{M}_{vv*}\cdot\mathbf{G}_{v*i}^c+\mathbf{M}_{vi}\end{aligned} \tag{26}$$

where

$$\mathbf{G}_{v*i}^c = \mathbf{Q}_{v*i}+\mathbf{Q}_{v*v}\cdot\mathbf{M}_{vi}. \tag{27}$$

This two-step simplification is valid because the magnitudes of $\mathbf{Q}_{v*i}$ and $\mathbf{Q}_{v*v}$ are small enough due to the droop slope n_q is very tiny according to (12). In the first step, the higher-order term, which refers to $(\mathbf{M}_{vv*}\cdot\mathbf{Q}_{v*v})^2$ here, is ignored. Similarly, in the second step, the higher-order term $(\mathbf{M}_{vv*}\cdot\mathbf{Q}_{v*v})\cdot(\mathbf{M}_{vv*}\cdot\mathbf{Q}_{v*i})$ is ignored. In this way, $\mathbf{G}_{v*i}^c$ is defined to represent the effect of *Q*–*V* droop-control on the terminal impedance $\mathbf{G}_{vi}$.

Second, since the cable impedance as well as the steady-state angle difference δ_0 is usually very small due to the limited length of cable, the transformation matrix $\mathbf{T}_s(\delta_0)$ in (20) can be treated as identity matrix in the following discussion. The terminal characteristics of Inv #1 and Invs #2 to #*N*, i.e., (21)–(24), can then be simplified as (28)–(31). The superscript " $'$ " is used for denoting the simplified form of terminal characteristics comparing to (21)–(24)

$$\mathbf{Z}'_o = -\mathbf{Z}_o^c \tag{28}$$

$$\mathbf{G}'_{\omega i} = -\mathbf{G}_{\omega i}^c \tag{29}$$

$$\mathbf{Y'}_o = -(\mathbf{Y}_o^c + \frac{(\mathbf{Y}_o^c \cdot \mathbf{T}_v + \mathbf{T}_c) \cdot \mathbf{G}_{\omega i}^c \cdot \mathbf{Y}_o^c}{s - \mathbf{G}_{\omega i}^c \cdot \mathbf{Y}_o^c \cdot \mathbf{T}_v}) \tag{30}$$

$$\mathbf{G'}_{i\omega} = \frac{\mathbf{Y}_o^c \cdot \mathbf{T}_v + \mathbf{T}_c}{s - \mathbf{G}_{\omega i}^c \cdot \mathbf{Y}_o^c \cdot \mathbf{T}_v}. \tag{31}$$

Finally, by substituting (31) into (30), the terminal admittance $\mathbf{Y'}_o$can be expressed in the form of the following equation:

$$\mathbf{Y'}_o = -(\mathbf{I} + \mathbf{G'}_{i\omega} \cdot \mathbf{G}_{\omega i}^c) \cdot \mathbf{Y}_o^c. \tag{32}$$

2) Effect of Droop-Control on Parallel Inverters: Based on the newly defined terminal characteristics $\mathbf{G}_{\omega i}^c$ and $\mathbf{G}_{v*i}^c$, which are used to describe the role of droop-control in the single inverter, the effect of droop-control on parallel inverters can be analyzed. In order to study the influence of outer power controller individually, other parameters, i.e., the inner loops as well as the cable impedances, of each inverter are assumed to be the same.

With the above simplifications, the overall block diagram of the interaction loops between parallel inverters can be depicted as Fig. 11(a) by unclosing each terminal characteristic in Fig. 10 and revealing every single part. For simplicity, the block diagram of a parallel system with only two grid-forming inverters is shown in Fig. 11(a), where Inv #1 is with voltage representation and Inv #2 is with the current representation. Meanwhile, the interaction between the inverters with the effects of the *P*–ω droop-control and the *Q*–*V* droop-control can be presented by separate paths.

It can be seen in Fig. 11(a) that *Q*–*V* droop-control introduces an additional term to the impedance of inner voltage and current loops $\mathbf{M}_{vi}$. However, the impedance shaping effect of *Q*–*V* droop-control is trivial comparing to the original impedance $\mathbf{M}_{vi}$ due to the tiny droop slope n_q and can be ignored.

Furthermore, since the magnitude of the impedance of inner voltage and current loops $|\mathbf{M}_{vi}|$ is very small due to tight voltage feedback regulation, $\mathbf{G}_{\omega i}^c$ can be simplified as (33) based on (17) and (26)

$$\mathbf{G}_{\omega i}^c \approx \mathbf{P}_{\omega i}. \tag{33}$$

Finally, since the steady-state capacitor voltage of *q*-axis V_{Cq}^c is fixed as 0, the active power *p* is only perturbed by *d*-axis current i_{od} according to (1), which means the second column element of the transfer function $\mathbf{P}_{\omega i}$ referring to *P*–ω droop-control will be 0 as can be observed in (11) and (34)

$$\mathbf{P}_{\omega i} \approx [P_{\omega id} \quad 0] \tag{34}$$

where

$$P_{\omega id} = -\frac{3}{2} m_p G_{\text{LPF}} V_{Cd}^c. \tag{35}$$

Based on the above discussions, Fig. 11(a) can be simplified to Fig. 11(b), noticing that the variables and transfer functions in the interaction path of the *P*–ω droop-control are all scalars except for the term $\mathbf{G'}_{i\omega 2}$. The models including power stage with inner voltage and current loops are encapsulated again as terminal impedance and admittance $\mathbf{Z}_{o1}^c$ and $\mathbf{Y}_{o2}^c$ in Fig. 11(b).

3) Feature Analysis on Interaction of Droop-Control Among Parallel Inverters: In order to further study the feature of the interaction of *P*–ω droop-control among parallel inverters, detailed observation is conducted.

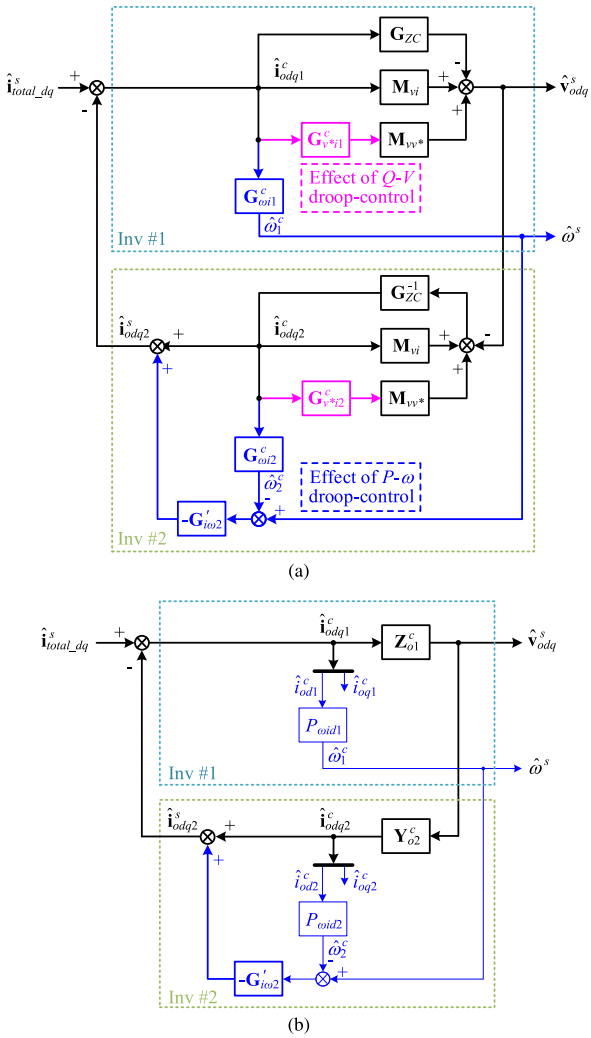

Fig. 11. Interaction paths between two parallel grid-forming inverters in forms of (a) block diagram with MIMO nature, and (b) simplified block diagram focusing on the effect of *P*–ω droop-control, where Inv #1 and Inv #2 are with the voltage representation and the current representation, respectively.

By substituting the simplified forms of terminal characteristics (28), (29), (31), (32), and (33) into (25), the return ratio matrix is calculated as

$$\begin{aligned}\mathbf{L} &= \sum_{k=2}^{N} (\mathbf{Y'}_{ok} \cdot \mathbf{Z'}_{o1} + \mathbf{G'}_{i\omega k} \cdot \mathbf{G'}_{\omega i1}) \\ &= \sum_{k=2}^{N} ((\mathbf{I} + \mathbf{G'}_{i\omega k} \cdot \mathbf{P}_{\omega ik}) \cdot \mathbf{Y}_{ok}^c \cdot \mathbf{Z}_{o1}^c - \mathbf{G'}_{i\omega k} \cdot \mathbf{P}_{\omega i1}) \\ &= (N-1) \cdot \mathbf{I} + \mathbf{L}_P \end{aligned} \tag{36}$$

where

$$\mathbf{L}_P = \sum_{k=2}^{N} (\mathbf{G'}_{i\omega k} \cdot (\mathbf{P}_{\omega ik} - \mathbf{P}_{\omega i1})). \tag{37}$$

Notice that $\mathbf{Y}_{ok}^c \cdot \mathbf{Z}_{o1}^c \approx \mathbf{I}$ here.

$\mathbf{L}_P$ can be used to describe the interaction of P–ω droop-control among the parallel inverters since the term $\mathbf{P}_{\omega i}$ is covered. Equation (36) indicates that if the effect of droop-control is not considered, the return ratio matrix will be a scalar matrix, implying an always stable system, since the characteristic loci of $\mathbf{L}$ are just two points at (N–1+j0), which will never encircle the critical point (–1+j0) definitely.

In (37), $\mathbf{L}_P$ is the sum of a series of product terms containing the differences of $\mathbf{P}_{\omega i}$ between Inv #k and Inv #1. It is obvious to find that if the control parameters, namely the active power-droop slope m_{pk} and the power LPF G_{LPFk} with the cutoff frequency ω_{fk} of Inv #k are in consistent with those of Inv #1, then the differences of $\mathbf{P}_{\omega i}$ will be zero and $\mathbf{L}_P$ will have no influence on the return ratio matrix $\mathbf{L}$ as well as on system stability.

Since the second column elements of $\mathbf{P}_{\omega i}$ in (34) are zero, the second column elements of $\mathbf{L}_P$ in (37) will still be zero after the premultiplication by $\mathbf{G'}_{i\omega k}$ as shown in the following equation:

$$\mathbf{L}_P = \begin{bmatrix} L_{Pdd} & L_{Pdq} \\ L_{Pqd} & L_{Pqq} \end{bmatrix} \approx \begin{bmatrix} L_{Pdd} & 0 \\ L_{Pqd} & 0 \end{bmatrix}. \tag{38}$$

In Fig. 11(b), the blue paths reflect the effect of $\mathbf{L}_P$. It can be observed from both Fig. 11(b) and (38) that $\mathbf{L}_P$ only has influence on the first column elements of $\mathbf{L}$ referring to the perturbation of d-axis current.

Then, the return ratio matrix can be calculated as follows by combining (36) and (38):

$$\begin{aligned} \mathbf{L} &\approx (N-1)\cdot\mathbf{I} + \mathbf{L}_P \\ &\approx \begin{bmatrix} (N-1)+L_{Pdd} & 0 \\ L_{Pqd} & (N-1) \end{bmatrix}. \end{aligned} \tag{39}$$

Equation (39) shows that the second column elements of the return ratio matrix will always be 0 and (N–1), respectively

$$\begin{cases} L_{dq} = 0 \\ L_{qq} = N-1. \end{cases} \tag{40}$$

C. Proposed SISO Stability Analysis Approach

The SISO stability analysis approach can be illustrated intuitively by the Gershgorin theorem.

The Gershgorin theorem gives the location of eigenvalues in s plane for a complex matrix [30]. Let matrix $\mathbf{A} = (a_{ij}) \in C^{n\times n}$, then its eigenvalues $\lambda_1, \lambda_2, \ldots\lambda_n$ are limited within n discs on the complex plane, as shown in the following equation:

$$S(\mathbf{A}) = \bigcup_{i=1}^{n} \left\{ \lambda : \ |\lambda - a_{ii}| \le R_i = \sum_{\substack{j=1 \\ j\neq i}}^{n} |a_{ji}| \right\}. \tag{41}$$

The ith Gershgorin disc corresponds to the elements in column i of matrix $\mathbf{A}$, with diagonal element a_{ii} as the center and the union of the off-diagonal elements $R_i = \sum_{\substack{j=1 \\ j\neq i}}^{n} |a_{ji}|$ as the radius.

In [21], a band area containing the eigenvalue loci is proposed, which indicates that if the Gershgorin disc radius is small enough, it will be possible to use the Nyquist loci of diagonal elements to approximate characteristic loci.

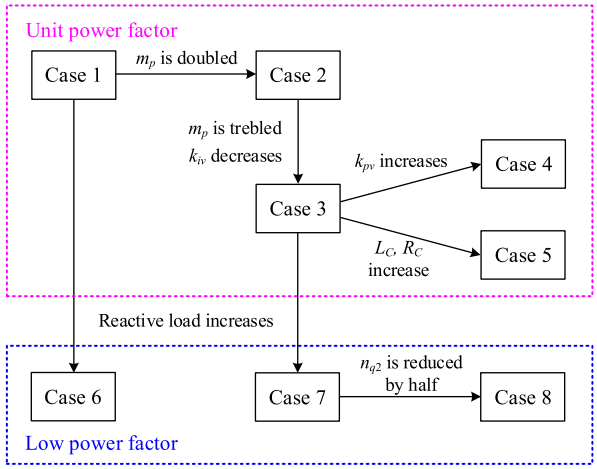

Fig. 12. Design principle of the representative eight case studies.

According to the Gershgorin theorem, the characteristic loci l_1, l_2 of two-dimensional matrix $\mathbf{L}$ lie in the union of two Gershgorin discs. Normally, the Gershgorin disc of d-d channel does not overlap with that of q-q channel. Therefore, the relationship between l_1, l_2 and four elements of $\mathbf{L}$ can be expressed by

$$\begin{cases} |l_1 - L_{dd}| \le |L_{qd}| \\ |l_2 - L_{qq}| \le |L_{dq}|. \end{cases} \tag{42}$$

In (42), the Gershgorin disc radii are $|L_{qd}|$ and $|L_{dq}|$ for l_1 and l_2, respectively. By applying the Gershgorin theorem to the transpose of $\mathbf{L}$, (42) is developed into the following equation:

$$\begin{cases} |l_1 - L_{dd}| \le \min\{|L_{dq}|, |L_{qd}|\} \\ |l_2 - L_{qq}| \le \min\{|L_{dq}|, |L_{qd}|\}. \end{cases} \tag{43}$$

Therefore, the Gershgorin disc radius of l_1 and l_2 is unified as $\min\{|L_{dq}|, |L_{qd}|\}$.

As discussed before, in a parallel grid-forming inverters system, the d-q and q-q elements of the return ratio matrix are fixed. Therefore, (44) can be obtained from (40) and (43)

$$\begin{cases} l_1 = L_{dd} \\ l_2 = L_{qq} = N-1. \end{cases} \tag{44}$$

Equation (44) shows that the characteristic loci will coincide with the Nyquist loci of diagonal elements since the Gershgorin disc radius is fixed as 0. Moreover, the characteristic locus l_2 will be constrained around the point (N–1+j0) and have no possibility to encircle (–1+j0). The stability of the parallel grid-forming inverters is dominated by the characteristic locus l_1 corresponding to d axes.

In summary, the original GNC-based stability criterion for parallel grid-forming inverters proposed in [28] is simplified and further developed into a SISO Nyquist criterion applied to d-d channel element L_{dd}. With this SISO approach, the complicated work to calculate the characteristic loci of the return ratio matrix $\mathbf{L}$ is exempted, which significantly reduces the computation complexity.

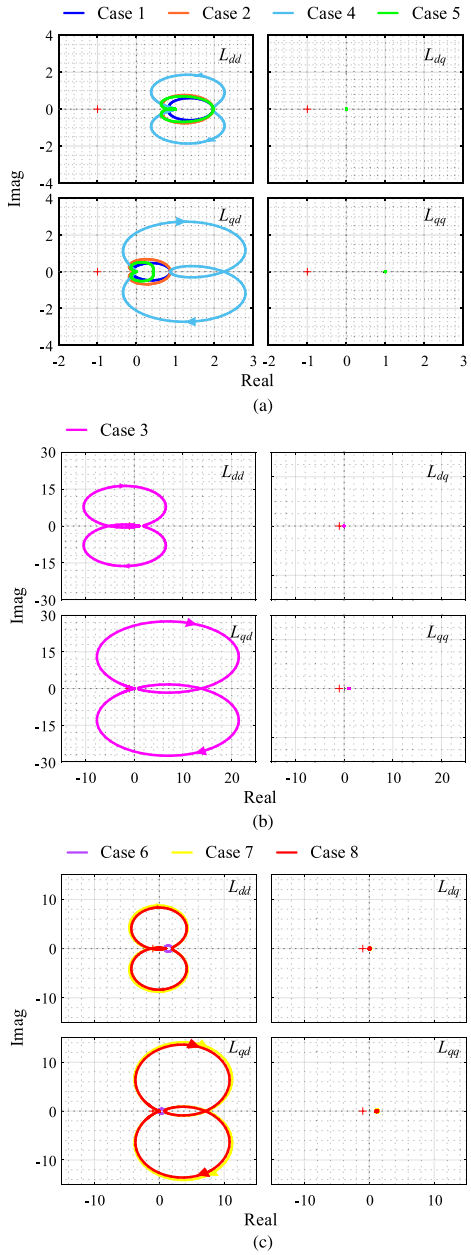

Fig. 13. Nyquist plots of four elements of the return ratio matrix **L** with (a) Cases 1, 2, 4, and 5; (b) Case 3; and (c) Cases 6–8.

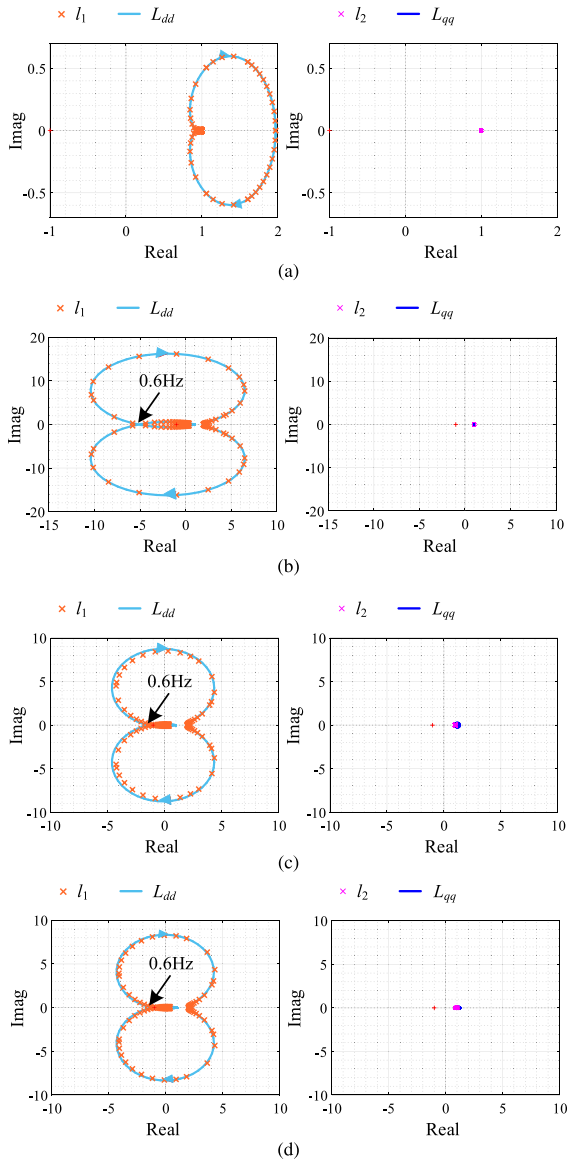

Fig. 14. Characteristic loci with loci of simplified expressions in different cases. (a) Case 1. (b) Case 3. (c) Case 7. (d) Case 8.

IV. Stability Analysis of Parallel Grid-Forming Inverters

A. Design of Representative Cases

In order to study the impacts of critical parameters changing and analyze the stability of parallel system comprehensively as well as to verify the proposed simplified stability analysis approach, eight representative case studies of an $N = 2$ inverter parallel system are designed, which are illustrated by Fig. 12. All parameters of two parallel inverters are set as base values in case 1. Compared to case 1, the active power droop slopes m_{p1} and m_{p2} are doubled in case 2 and then trebled in case 3. The integral gain k_{iv1} and k_{iv2} of voltage PI controller of two inverters decrease simultaneously in case 3, and case 3 will therefore be an unstable case. In cases 4 and 5, the active power droop slopes m_{p1} and m_{p2} keep the same as those in case 3. In case 4, the proportional gain k_{pv1} and k_{pv2} of voltage PI controller of two inverters increase. In case 5, the cable impedance L_C and R_C increase. Cases 1–5 share one common working condition with unit PF. Cases 6–8 are designed to verify the feasibility of the SISO analysis approach in condition of nonunity PF operation. The control parameters of cases 6 and 7 are the same as cases 1 and 3, respectively, whereas in case 8, the reactive power droop slope n_{q2} is reduced by half. The detailed parameters of eight cases are listed in the Appendix.

The eight cases cover possible changing trends and combinations of parameters from both outer power droop-control and inner dominant voltage control. By systematically designing these eight cases, not only the impacts of individual parameters are revealed but also their combined effects are investigated, which covers the general operating conditions of parallel grid-forming inverters.

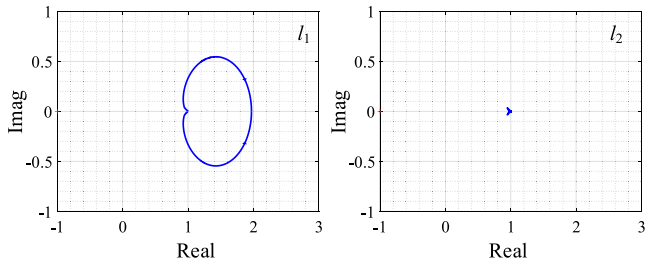

Fig. 15. Characteristic loci of the system return ratio matrix **L** with simplified model neglecting inner control loops in case 3.

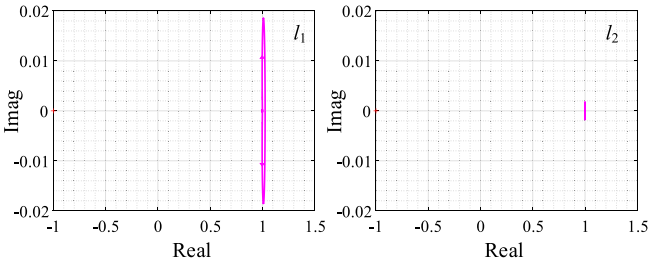

Fig. 16. Characteristic loci of the system return ratio matrix **L** with simplified model ignoring outer power droop-control in case 3.

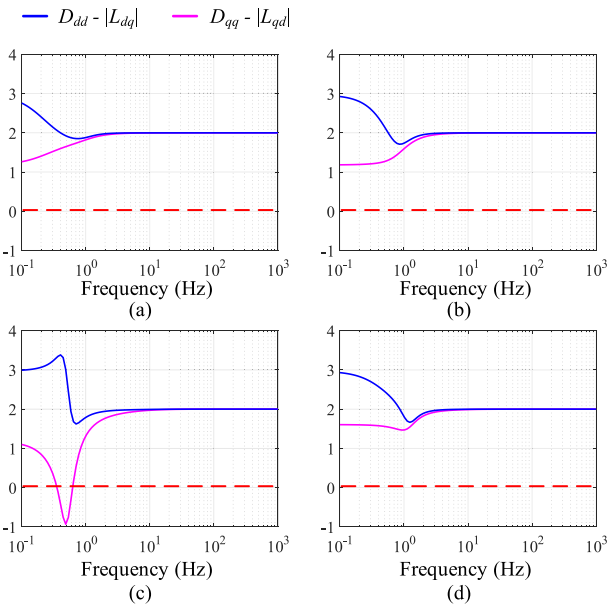

Fig. 17. Stability predicting results using the simplified stability criterion proposed in [21] in (a) Case 1, (b) Case 2, (c) Case 4, and (d) Case 5.

B. Stability Analysis of Eight Cases

In eight cases, the Nyquist plots of four elements of return ratio matrix **L** are drawn in Fig. 13. The simplified expression L_{dd} has been proved to be a good approximation of the characteristic loci l_1 in the previous discussion, the system stability can therefore be predicted by the encirclement of (–1+j0) by the Nyquist locus of L_{dd}. In Fig. 13(a), the Nyquist plots of L_{dd} all lie in the RHP, predicting the parallel system to be stable in cases 1, 2, 4, and 5. In Fig. 13(b), the Nyquist plots of L_{dd} encircle (–1+j0), which indicates the system loses stability in case 3. Fig. 13(c) draws the Nyquist plots of cases 6–8 at nonunity PF operation, in which case 6 is predicted to be stable and cases 7 and 8 are predicted to be unstable.

In addition, the conclusion of $L_{dq} = 0$ and $L_{qq} = (N–1)$ is also verified with the Nyquist plots of different cases shown in the figure.

The characteristic loci together with the Nyquist loci are plotted in Fig. 14. When applying GNC, the frequency at the intersection point of characteristic loci and the left-half real axis is recognized as the approximate resonant frequency of the unstable system. In the designed eight cases, case 3 is an unstable case at unity PF operation, whereas cases 7 and 8 are unstable cases at nonunity PF operation. The frequency at the intersection point in unstable case is also displayed in Fig. 14.

In Fig. 14, l_2 is always around (1+j0) as proved before, indicating it has no possibility to encircle (–1+j0). The Nyquist plot of L_{dd} is in good agreement with the characteristic loci l_1 in case 3 of unity PF operation. In cases 7 and 8 of nonunity PF operation, there is a little difference between L_{dd} and l_1, which is caused by the approximation of $|L_{dq}| = 0$.

In Fig. 14, the frequency at the intersection point of left-half real axis and L_{dd} is equal to 0.6 Hz. The oscillation frequencies in three cases are therefore predicted to be 0.6 Hz, which will be verified in experiments.

C. Comparison With Existing Simplified Models

As discussed in Section I, existing small-signal impedance models of the grid-forming inverter are simplified in two different ways [22], [23], [24], [25], [26], neglecting the inner voltage and current control loops or ignoring outer power droop-control loop. These simplified models are not accurate to reflect the comprehensive terminal dynamics of grid-forming inverter and cannot accurately predict system stability. In order to prove the effectiveness of the proposed accurate model, the comparison between the proposed model and existing simplified models are conducted.

According to the analysis results in the previous section, case 3 is predicted to be unstable using the proposed model. The simplified model neglecting inner control loops presented in [22] and [23] is first applied to case 3. In this simplified model, the dynamics of inner capacitor voltage and inductor current control loops are neglected, which are idealized as a unit gain block. According to the modeling process of inner voltage and current loops in Section II-B, the transfer functions in (10) should be $\mathbf{M}_{vv*} = \mathbf{I}$, $\mathbf{M}_{vi} = \mathbf{0}$ for the simplified model. Substituting simplified (10) into (21)–(24) and calculating $\mathbf{Z}_{o1}$, $\mathbf{G}_{\omega i1}$ and $\mathbf{Y}_{o2}$, $\mathbf{G}_{i\omega 2}$, the return ratio matrix **L** in (25) can be calculated, whose characteristic loci are shown in Fig. 15. The characteristic loci do not encircle (–1+j0), based on GNC, the parallel system is predicted to be stable in case 3 using a simplified model.

The simplified model ignoring outer power droop-control in [24], [25], and [26] is then tested in case 3. In this simplified model, the droop-control scheme is eliminated. The active and reactive power droop slopes m_p, n_q cannot function and be equivalent to constant 0. In this condition, the inverter fundamental frequency no longer varies with output active power and

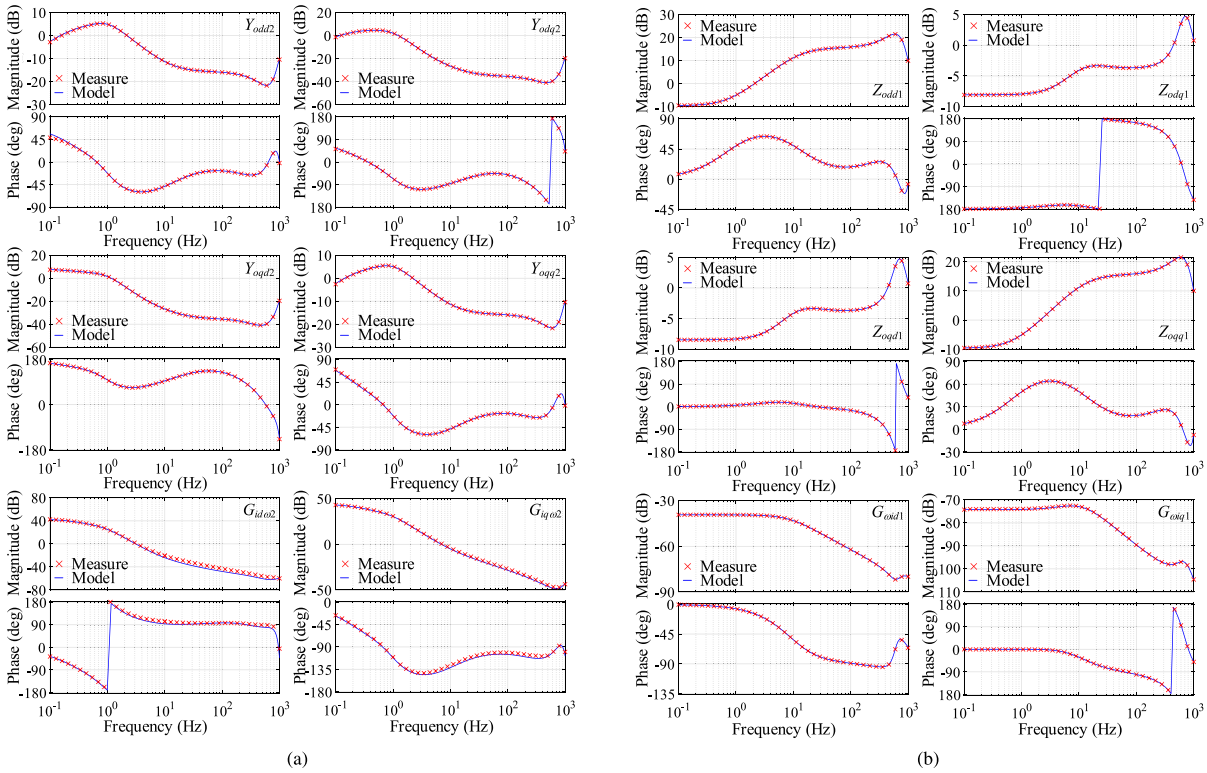

Fig. 18. Bode plots of measured and proposed inverter terminal characteristics of (a) Inv #1 with voltage representation and (b) Inv #2 with current representation.

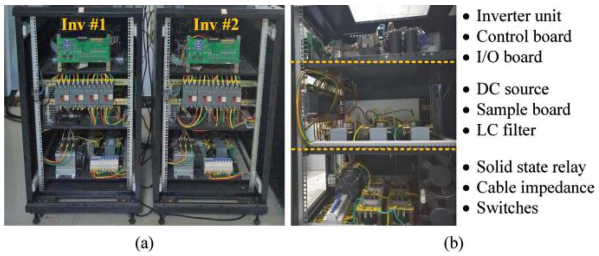

Fig. 19. Hardware platform of two parallel inverters. (a) Overall view. (b) Inside view of each inverter.

always equal to rated value ω_0. Since the fundamental frequency does not have any dynamics, terminal characteristics $\mathbf{G}_{\omega i1}$ and $\mathbf{G}_{i\omega 2}$ are invalid. In (25), only $\mathbf{Y}_{o2}\cdot\mathbf{Z}_{o1}$ is left in system return ratio matrix $\mathbf{L}$. In this condition, the characteristic loci of $\mathbf{L}$ are calculated and plotted in Fig. 16. The critical point $(-1+\mathrm{j}0)$ is not encircled, indicating a stable parallel system.

In summary, the parallel system in case 3 is predicted to be stable using the simplified models both in [22], [23], [24], [25], [26], which is conflicting to the prediction result using the proposed full model. The actual system stability of total eight cases can be verified by the experimental results in the following section.

D. Comparison With Existing Simplified Stability Criterion

When applying the simplified stability criterion proposed in [21], a three-phase ac system is predicted to be stable only when the following conditions hold.

1) Neither Nyquist loci of diagonal element L_{dd} nor the one of L_{qq} encircles (-1+j0).
2) At each frequency, the distance D_{dd} between L_{dd} and (-1+j0) in the complex plane is longer than $|L_{dq}|$, and the distance D_{qq} between L_{qq} and (-1+j0) in the complex plane is larger than $|L_{qd}|$, shown as follows:

$$\begin{cases} D_{dd} = |L_{dd}+1| > |L_{dq}| \\ D_{qq} = |L_{qq}+1| > |L_{qd}| \end{cases}. \tag{45}$$

If either of the two requirements is not met, the system is predicted to be unstable.

Fig. 17 shows the predicting results using the above simplified stability criterion in cases 1, 2, 4, and 5, which are all predicted to be stable using the stability criterion proposed in this article as well as GNC. The Nyquist loci of L_{dd} and L_{qq} can be observed in Fig. 13(a).

It can be found that in cases 1, 2, and 5, the system is predicted to be stable whether using GNC or the stability criterion in [21]. In case 4, however, (45) is not satisfied for every frequency as shown in Fig. 17(c), since the influence of off-diagonal element L_{qd} is significant. Thus, the system is predicted to be unstable using the simplified stability criterion presented in [21], which is conflicting to the prediction result of GNC. Therefore, the conservative stability criterion may lose the applicability when applied to parallel grid-forming inverters in islanded microgrids.

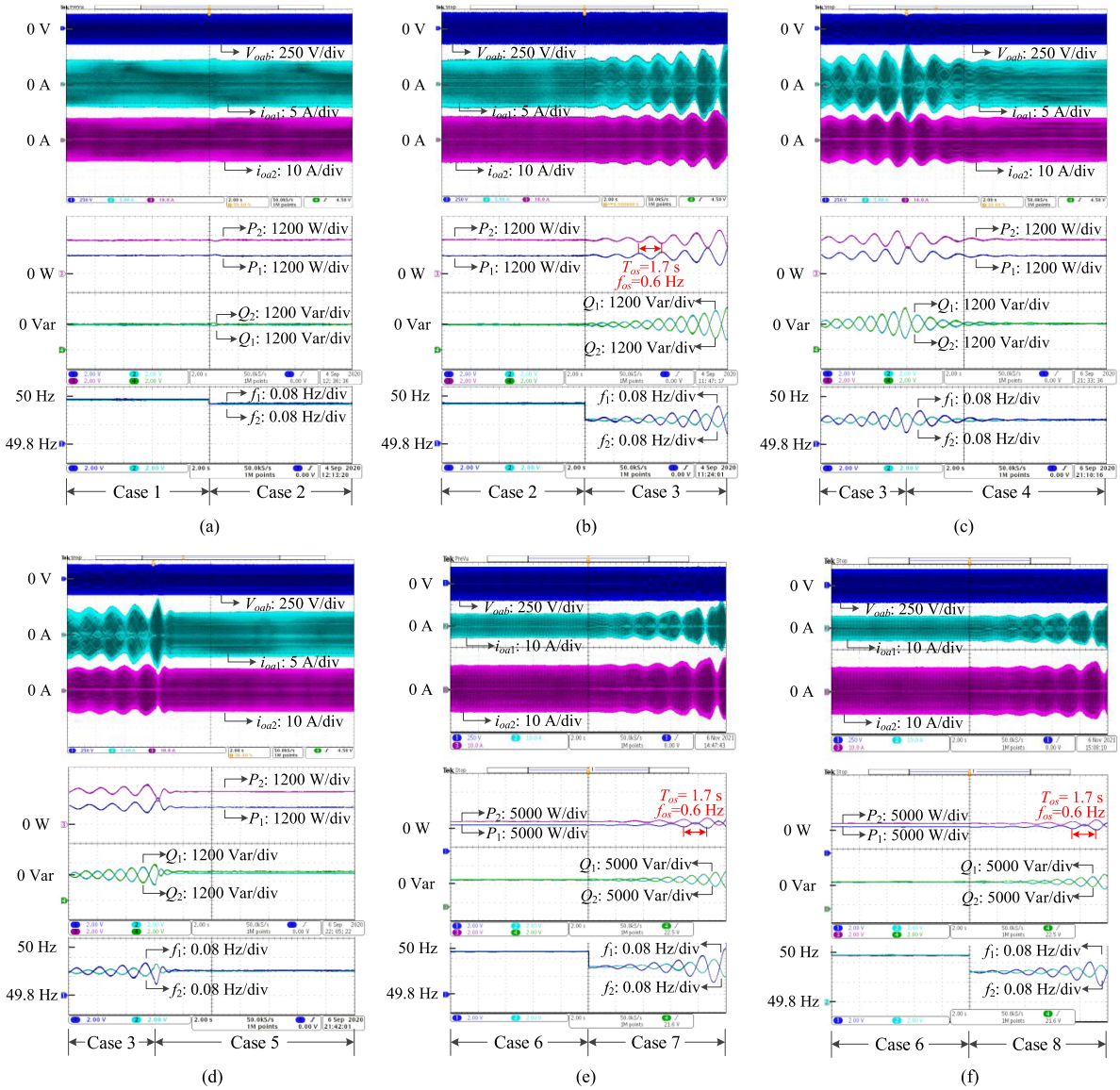

Fig. 20. Experimental waveforms of parallel Inv #1 and Inv #2 in cases 1–8. CH1, line-to-line PCC voltage, v_{oab}; CH2, Inv #1 output current, i_{oa1}; CH3, Inv #2 output current, i_{oa2}; CH4, Inv #1 active power, P_1; CH5, Inv #2 active power, P_2; CH6, Inv #1 reactive power, Q_1; CH7, Inv #2 reactive power, Q_2; CH8, Inv #1 fundamental frequency, f_1^c; CH9, Inv #2 fundamental frequency, f_2^c.

V. Simulation and Experimental Verification

A. Verification of Small-Signal Terminal Characteristics Model

In order to verify the accuracy of the proposed terminal characteristic model, the time-domain measurements are conducted in SABER. For $\mathbf{Z}_{o1}$, $\mathbf{G}_{\omega i1}$ of Inv #1 with voltage representation, a shunt current perturbation is injected. The response signals are the *dq*-voltage amplitude and fundamental frequency. For $\mathbf{Y}_{o2}$, $\mathbf{G}_{i\omega 2}$ of Inv #2 with current representation, the perturbation signals are the amplitude and fundamental frequency of a series-connected voltage source, whereas the response signal is the *dq*-output current. The detailed procedures of measuring these terminal characteristics are presented in [28]. Due to the limited space, the measurement results of $\mathbf{Z}_{o1}$, $\mathbf{G}_{\omega i1}$ and $\mathbf{Y}_{o2}$, $\mathbf{G}_{i\omega 2}$ in eight cases cannot all be presented. The time-domain measurement results of case 1 are shown in Fig. 18, which serves as an example to validate the accuracy of theoretical model. It can be observed that the Bode plots of transfer functions of inverter terminal characteristics derived in Section II coincide well with the time-domain measurement results, which confirms that the proposed theoretical model is accurate to reflect the terminal dynamics of grid-forming inverters.

B. Verification of SISO Stability Analysis Approach

The experiment platform of two parallel inverters is shown in Fig. 19. The inner structure of each inverter consists of three layers. As Fig. 19(b) shows, the first layer contains a three-phase

inverter unit MWINV-9R144, control board, and I/O board. At the second layer, a programmable dc source feeds to the dc side of the inverter, providing 600 V dc voltage. The sample board and *LC* filter are also included in this layer. Single inverter is connected to the PCC through a solid state relay and cable impedance in the third layer. The power stage and control scheme of each inverter in the hardware platform are the same as Fig. 1. The parameters of Inv #1 and Inv #2 are in accordance with the data listed in the Appendix.

First, the unit PF working condition: $P_{out1}\approx$1kW, $P_{out2}\approx$2kW, $Q_{out1}\approx Q_{out2}\approx$0kVar corresponding to cases 1–5 is conducted. The three-phase programmable electronic load Chroma 63804 is operated in constant current mode, serving as the current sink and absorbing active power. The experimental waveforms of cases 1 and 2 are shown in Fig. 20(a). The top three channels are ac components: PCC voltage v_{oab}, Inv #1 output current i_{oa1}, and Inv #2 output current i_{oa2}. The middle four channels are output active and reactive powers of Inv #1 and Inv #2: P_1, P_2 and Q_1, Q_2. The bottom two channels are fundamental frequencies of Inv #1 and Inv #2: $f_1^c$and f_2^c. The output powers and fundamental frequencies are obtained from the control programs and converted to 0-5 V voltage by D/A.

In cases 1 and 2, the amplitudes of PCC voltage, output currents and output powers of two inverters are constant, indicating the stable operation of parallel system. Since the active power droop slopes m_{p1} and m_{p2} are doubled, the steady-state fundamental frequencies decrease from 49.9984 Hz in case 1 to 49.9968 Hz in case 2.

In case 3, the active power droop slopes m_{p1} and m_{p2} are further increased to six times of base value with integral gain of voltage PI controller k_{iv1} and k_{iv2} decreasing from 15 to 6 simultaneously; it can be observed from Fig. 20(b) that as all waveforms begin to oscillate divergently, the system loses stability. The oscillation period of dc components P_1, P_2, Q_1, Q_2 and f_1^c, $f_2^c$is around 1.7 s, indicating an oscillation frequency of 0.6 Hz approximately, which is in consistent with predictions in Section IV-B.

Then, the voltage proportional control parameters of two inverters, k_{pv1} and k_{pv2} are increased from 0.1 to 0.8. As Fig. 20(c) shows, when transformed to case 4 at time = 6 s, the oscillations of waveforms begin to attenuate. After several oscillation cycles, the system recovers stable operation.

The parameters of case 5 are the same as case 3 except for larger cable impedance L_C and R_C. In the experiment platform, inductor and resistor are series connected between the inverter output terminal and PCC to emulate the distribution cable impedance in real engineering applications. As Fig. 20(d) shows, the initial case 3 is unstable. Then, another inductor L_C = 3.3 mH with ESR $R_C = 0.08\ \Omega$ is connected into the circuit. The parallel system become stable immediately with total $L_C =$ 4.5 mH and $R_C = 0.41\ \Omega$.

Finally, the nonunity PF working condition: $P_{out1}\approx$1 kW, $P_{out2}\approx$2 kW, $Q_{out1}\approx Q_{out2}\approx$1 kVar corresponding to cases 6–8 is verified. Since the sink current waveform of electronic load Chroma 63804 is not sinusoidal when PF $<$ 1, it is replaced by Chroma B61860 with regenerative ac load function. The constant current phase lag mode of Chroma B61860 can sink sinusoidal current with PF $<$ 1. As Fig. 20(e) and (f) shows, oscillations can still be observed with added reactive load current, indicating the parallel system is unstable. The oscillation period is about 1.7 s with the oscillation frequency being 0.6 Hz, also in consistent with predictions.

In summary, using the proposed accurate terminal characteristic model and SISO approach, the stability predictions of eight cases all coincide with the time-domain experimental results. For case 3, the parallel system is unstable in experiments but predicted to be stable using existing simplified models, which suggests that simplified models are not accurate and cannot be applied to predict system stability.

VI. Conclusion

This article proposes a small-signal terminal characteristic model for grid-forming inverters, considering the dynamic interaction of fundamental frequency and covering the dynamics of outer power control loop, inner voltage and current control loops, *LC* filter, and distribution cable impedance, which is more accurate than existing models neglecting the inner voltage and current control loops or ignoring outer power droop-control loop. Furthermore, by analyzing the mathematical feature of the terminal characteristics model proposed, this article decomposes the return ratio of the parallel grid-forming inverters into two key parts, which represent the interaction among *P*–ω droop-control of parallel inverters and the interaction among *Q*–*V* droop-control of parallel inverters, respectively, and the former one is dominated. Thus, the conventional Nyquist criterion can be implemented to *d*-*d* channel element of return ratio matrix to predict the stability of parallel grid-forming inverters. Compared to the GNC-based criterion, this SISO approach avoids the calculation of characteristic loci and reduces computation complexity. In different operating cases, experimental results prove the accuracy of theoretical predictions, validating the effectiveness of the proposed terminal characteristic model and SISO stability analysis approach.

Appendix

Parameters of Inverters in Eight Cases

TABLE I
Fixed and Common Parameters of Inv #1 and Inv #2

Symbol	Description	Value
V_{dc}	DC voltage	600 V
L_f	Filter inductor	3.6 mH
r_{Lf}	ESR of filter inductor	0.08 Ω
C_f	Filter capacitor	30 μF
ω_f	Cut-off frequency of power LPF	2π·10 rad/s
ω_0	Rated fundamental frequency	2π·50 rad/s
V_0	Rated voltage amplitude	115.5 V
P_0	Active power bias	0 W
Q_0	Reactive power bias	0 Var
k_{pc}	Proportional gain of current controller	0.04/A

TABLE II
CHANGING PARAMETERS OF INVERTERS IN EIGHT CASES

Symbol	Description	Unit	1	2	3	4	5	6	7	8
m_{p1}	Active power droop slope of Inv #1	rad/(s·W)	6.4×10^{-5}	1.28×10^{-4}	4×10^{-4}	4×10^{-4}	4×10^{-4}	6.4×10^{-5}	4×10^{-4}	4×10^{-4}
m_{p2}	Active power droop slope of Inv #2	rad/(s·W)	3.2×10^{-5}	6.4×10^{-5}	2×10^{-4}	2×10^{-4}	2×10^{-4}	3.2×10^{-5}	2×10^{-4}	2×10^{-4}
n_{q1}	Reactive power droop slope of Inv #1	V/Var	1×10^{-4}	1×10^{-4}	1×10^{-4}	1×10^{-4}	1×10^{-4}	1×10^{-4}	1×10^{-4}	1×10^{-4}
n_{q2}	Reactive power droop slope of Inv #2	V/Var	1×10^{-4}	1×10^{-4}	1×10^{-4}	1×10^{-4}	1×10^{-4}	1×10^{-4}	1×10^{-4}	5×10^{-5}
k_{pv1}=k_{pv2}	Proportional gain of voltage controller	A/V	0.1	0.1	0.1	0.8	0.1	0.1	0.1	0.1
k_{iv1}=k_{iv2}	Integral gain of voltage controller	A/(V·s)	15	15	6	6	6	15	6	6
L_{C1}=L_{C2}	Distribution cable inductance	mH	1.2	1.2	1.2	1.2	4.5	1.2	1.2	1.2
R_{C1}=R_{C2}	Distribution cable resistance	Ω	0.33	0.33	0.33	0.33	0.41	0.33	0.33	0.33

REFERENCES

[1] J. M. Carrasco et al., "Power-electronic systems for the grid integration of renewable energy sources: A survey," *IEEE Trans. Ind. Electron.*, vol. 53, no. 4, pp. 1002–1016, Jun. 2006.

[2] B. Kroposki, C. Pink, R. DeBlasio, H. Thomas, M. Simões, and P. K. Sen, "Benefits of power electronic interfaces for distributed energy systems," *IEEE Trans. Energy Convers.*, vol. 25, no. 3, pp. 901–908, Sep. 2010.

[3] M. C. Chandorkar, D. M. Divan, and R. Adapa, "Control of parallel connected inverters in standalone AC supply systems," *IEEE Trans. Ind. Appl.*, vol. 29, no. 1, pp. 136–143, Jan./Feb. 1993.

[4] J. Rocabert, A. Luna, F. Blaabjerg, and P. Rodríguez, "Control of power converters in ac microgrids," *IEEE Trans. Power Electron.*, vol. 27, no. 11, pp. 4734–4749, Nov. 2012.

[5] P. Huang, P. Vorobev, M. A. Hosani, J. L. Kirtley, and K. Turitsyn, "Plug-and-play compliant control for inverter-based microgrids," *IEEE Trans. Power Syst.*, vol. 34, no. 4, pp. 2901–2913, Jul. 2019.

[6] E. Coelho, P. Cortizo, and P. Garcia, "Small-signal stability for parallel connected inverters in stand-alone AC supply systems," *IEEE Trans. Ind. Appl.*, vol. 38, no. 2, pp. 533–542, Mar./Apr. 2002.

[7] N. Pogaku, M. Prodanovic, and T. C. Green, "Modeling, analysis and testing of autonomous operation of an inverter-based microgrid," *IEEE Trans. Power Electron.*, vol. 22, no. 2, pp. 613–625, Mar. 2007.

[8] K. Yu, Q. Ai, S. Wang, J. Ni, and T. Lv, "Analysis and optimization of droop-controller for microgrid system based on small-signal dynamic model," *IEEE Trans. Smart Grid*, vol. 7, no. 2, pp. 695–705, Mar. 2016.

[9] S. Hiti, V. Vlatkovic, D. Boroyevich, and F. C. Lee, "A new control algorithm for three-phase PWM buck rectifier with input displacement factor compensation," *IEEE Trans. Power Electron.*, vol. 9, no. 2, pp. 173–180, Mar. 1994.

[10] J. Sun, "Input impedance analysis of single-phase PFC converters," *IEEE Trans. Power Electron.*, vol. 20, no. 2, pp. 308–314, Mar. 2005.

[11] J. Sun, "Small-signal methods for AC distributed power systems—A review," *IEEE Trans. Power Electron.*, vol. 24, no. 11, pp. 2545–2554, Nov. 2009.

[12] A. MacFarlane and I. Postlethwaite, "The generalized Nyquist stability criterion and multivariable root loci," *Int. J. Control*, vol. 25, no. 1, pp. 81–127, Feb. 1977.

[13] M. Belkhayat, "Stability criteria for AC power systems with regulated loads," Ph.D. dissertation, Purdue Univ., West Lafayette, IN, USA, Dec. 1997.

[14] B. Wen, D. Boroyevich, R. Burgos, P. Mattavelli, and Z. Shen, "Analysis of D-Q small-signal impedance of grid-tied inverters," *IEEE Trans. Power Electron.*, vol. 31, no. 1, pp. 675–687, Jan. 2016.

[15] X. Wang, L. Harnefors, and F. Blaabjerg, "Unified impedance model of grid-connected voltage-source converters," *IEEE Trans. Power Electron.*, vol. 33, no. 2, pp. 1775–1787, Feb. 2018.

[16] H. Mao, D. Boroyevich, and F. C. Y. Lee, "Novel reduced-order small-signal model of a three-phase PWM rectifier and its application in control design and system analysis," *IEEE Trans. Power Electron.*, vol. 13, no. 3, pp. 511–521, May 1998.

[17] R. Burgos, D. Boroyevich, F. Wang, K. Karimi, and G. Francis, "On the AC stability of high power factor three-phase rectifiers," in *Proc. IEEE 2nd Energy Convers. Congr. Expo.*, Atlanta, GA, USA, 2010, pp. 2047–2054.

[18] H. Zhang, L. Harnefors, X. Wang, H. Gong, and J. Hasler, "Stability analysis of grid-connected voltage-source converters using SISO modeling," *IEEE Trans. Power Electron.*, vol. 34, no. 8, pp. 8104–8117, Aug. 2019.

[19] B. Wen, R. Burgos, D. Boroyevich, P. Mattavelli, and Z. Shen, "AC stability analysis and *dq* frame impedance specifications in power-electronics-based distributed power systems," *IEEE J. Emerg. Sel. Topics Power Electron.*, vol. 5, no. 4, pp. 1455–1465, Dec. 2017.

[20] H. Liu, X. Xie, and W. Liu, "An oscillatory stability criterion based on the unified dq-frame impedance network model for power systems with high-penetration renewables," *IEEE Trans. Power Syst.*, vol. 33, no. 3, pp. 3472–3485, May 2018.

[21] Y. Ren et al., "A strictly sufficient stability criterion for grid-connected converters based on impedance models and Gershgorin's theorem," *IEEE Trans. Power Del.*, vol. 35, no. 3, pp. 1606–1609, Jun. 2020.

[22] S. Iyer, M. Belur, and M. Chandorkar, "A generalized computational method to determine stability of a multi-inverter microgrid," *IEEE Trans. Power Electron.*, vol. 25, no. 9, pp. 2420–2432, Sep. 2010.

[23] Z. Liu, J. Liu, D. Boroyevich, R. Burgos, and T. Liu, "Small-signal terminal characteristics modeling of three-phase droop-controlled inverters," in *Proc. 8th IEEE Energy Convers. Congr. Expo.*, Milwaukee, WI, USA, 2016, pp. 1–7.

[24] J. M. Guerrero, L. Garcia de Vicuna, J. Matas, M. Castilla, and J. Miret, "Output impedance design of parallel-connected UPS inverters with wireless load-sharing control," *IEEE Trans. Ind. Electron.*, vol. 52, no. 4, pp. 1126–1135, Aug. 2005.

[25] A. A. A. Radwan and Y. A. I. Mohamed, "Stabilization of medium-frequency modes in isolated microgrids supplying direct online induction motor loads," *IEEE Trans. Smart Grid*, vol. 5, no. 1, pp. 358–370, Jan. 2014.

[26] Q. Liu, Y. Tao, X. Liu, Y. Deng, and X. He, "Voltage unbalance and harmonics compensation for islanded microgrid inverters," *IET Power Electron.*, vol. 7, no. 5, pp. 1055–1063, May 2014.

[27] A. Bolzoni, G. M. Foglia, L. Frosio, M. F. Iacchetti, and R. Perini, "Impact of line and control parameters on droop stability in inverters for distributed generation," *IEEE Trans. Smart Grid*, vol. 9, no. 6, pp. 6656–6665, Nov. 2018.

[28] S. Wang, Z. Liu, J. Liu, D. Boroyevich, and R. Burgos, "Small-signal modeling and stability prediction of parallel droop-controlled inverters based on terminal characteristics of individual inverters," *IEEE Trans. Power Electron.*, vol. 35, no. 1, pp. 1045–1063, Jan. 2020.

[29] W. Cao, Y. Ma, F. Wang, L. M. Tolbert, and Y. Xue, "Low-frequency stability analysis of inverter-based islanded multiple-bus AC microgrids based on terminal characteristics," *IEEE Trans. Smart Grid*, vol. 11, no. 5, pp. 3662–3676, Sep. 2020.

[30] I. Postlethwaite and A. G. J. MacFarlane, *A Complex Variable Approach to the Analysis of Linear Multivariable Feedback Systems*. Berlin, Germany: Springer, 1979.

Jiajun Yu received the B.S. degree in electrical engineering, in 2020, from Xi'an Jiaotong University, Xi'an, China, where he is currently working toward the M.S. degree in electrical engineering.

His research interests include small-signal modeling and stability of ac microgrids.

Shike Wang (Member, IEEE) received the B.S. and Ph.D. degrees in electrical engineering from Xi'an Jiaotong University, Xi'an, China, in 2014 and 2020, respectively.

She then joined China Resources Power Technology Research Institute Co., Ltd., Shenzhen, China, as an R&D Engineer in energy storage and renewable energy generation. Her research interests include power grid and source coordination, and small-signal stability of power electronics systems.

Dr. Wang was the recipient of the First Prize Paper Award in 2021 IEEE TRANSACTIONS ON POWER ELECTRONICS.

Zeng Liu (Senior Member, IEEE) received the B.S. degree in electrical engineering from Hunan University, Changsha, China, in 2006, and the M.S. and Ph.D. degrees in electrical engineering from Xi'an Jiaotong University (XJTU), Xi'an, China, in 2009 and 2013, respectively.

He then joined, as a faculty member in electrical engineering, XJTU, where he is currently an Associate Professor. From 2015 to 2017, he was with the Center for Power Electronics Systems, Virginia Polytechnic Institute and State University, Blacksburg, VA, USA, as a Visiting Scholar. His research interests include control and stability of power electronics systems with multiple converters for renewable energy and energy storage applications.

Dr. Liu was the recipient of two Prize Paper Awards in the IEEE TRANSACTIONS ON POWER ELECTRONICS. He is currently an Associate Editor for the IEEE OPEN JOURNAL OF POWER ELECTRONICS and on the Editorial Board for the *Energies*, and was a Secretary General for 2019 IEEE 10th International Symposium on Power Electronics for Distributed Generation Systems and 2020 4th International Conference on HVDC.

Jiarui Li (Student Member, IEEE) received the B.S. degree in electrical engineering, in 2021, from Xi'an Jiaotong University, Xi'an, China, where he is currently working toward the Ph.D. degree in electrical engineering.

His research interests include modeling, control, and stability analysis of power electronic systems.

Jinjun Liu (Fellow, IEEE) received the B.S. and Ph.D. degrees in electrical engineering from Xi'an Jiaotong University (XJTU), Xi'an, China, in 1992 and 1997, respectively.

He then joined the XJTU Electrical Engineering School as a Faculty. From late 1999 to early 2002, he was with the Center for Power Electronics Systems, Virginia Polytechnic Institute and State University, Blacksburg, VA, USA, as a Visiting Scholar. In late 2002, he was promoted to a Full Professor and then the Head of the Power Electronics and Renewable Energy Center, XJTU, which now comprises more than 20 faculty members and more than 200 graduate students and carries one of the leading power electronics programs in China. From 2005 to early 2010, he was an Associate Dean of Electrical Engineering School, XJTU, and from 2009 to early 2015, the Dean for Undergraduate Education of XJTU. He is currently an XJTU Distinguished Professor of power electronics. He coauthored three books (including one textbook), published more than 500 technical papers in peer-reviewed journals and conference proceedings, holds more than 70 invention patents (China/U.S./EU), and delivered for many times plenary keynote speeches and tutorials at IEEE conferences or China national conferences. His research interests include modeling, control, and design methods for power converters and electronified power systems, power quality control and utility applications of power electronics, and microgrids for sustainable energy and distributed generation.

Dr. Liu was the recipient of many times governmental awards at national level or provincial/ministerial level for scientific research/teaching achievements. He was also the recipient of 2006 Delta Scholar Award, the 2014 Chang Jiang Scholar Award, the 2014 Outstanding Sci-Tech Worker of the Nation Award, the 2016 State Council Special Subsidy Award, the IEEE Transactions on Power Electronics 2016 and 2021 Prize Paper Awards, the Nomination Award for the Grand Prize of 2020 Bao Steel Outstanding Teacher Award, and the 2022 Fok Ying Tung Education and Teaching Award. He was the IEEE Power Electronics Society Region 10 Liaison and then China Liaison for 10 years, an Associate Editor for the IEEE TRANSACTIONS ON POWER ELECTRONICS since 2006, 2015–2019 Executive Vice President and 2020–2021 Vice President of IEEE PELS. He was on the Board of China Electrotechnical Society 2012–2020 and was elected the Vice President in 2013 and the Secretary General in 2018 of the CES Power Electronics Society. He was 2013–2021 Vice President for International Affairs, China Power Supply Society (CPSS), and since 2016, the inaugural Editor-in-Chief for *CPSS Transactions on Power Electronics and Applications*. He was elected the President of CPSS in November 2021. Since 2013, he has been the Vice Chair of the Chinese National Steering Committee for College Electric Power Engineering Programs.

Jiayu Shang received the B.S. degree in new energy science and engineering from Harbin Institute of Technology, Weihai, China, in 2022. She is currently working toward the M.S. degree in electrical engineering with Xi'an Jiaotong University, Xi'an, China.

Her research interests include modeling and stability analysis of power electronics systems.